Journal of Power Sources 490 (2021) 229537

Contents lists available at ScienceDirect

Journal of Power Sources

journal homepage: www.elsevier.com/locate/jpowsour

Operando calorimetry informs the origin of rapid rate performance in microwave-prepared $TiNb_2O_7$ electrodes

Sun Woong Baek [a], Kira E. Wyckoff [b], Danielle M. Butts [c], Jadon Bienz [d], Ampol Likitchatchawankun [e], Molleigh B. Preefer [d], Matevž Frajnkovič [a], Bruce S. Dunn [c,f], Ram Seshadri [b,d], Laurent Pilon [a,f,g,*]

[a] *Mechanical and Aerospace Engineering Department, Henry Samueli School of Engineering and Applied Science, University of California, Los Angeles, CA 90095, USA*
[b] *Materials Department, and Materials Research Laboratory, University of California, Santa Barbara, CA 93106, USA*
[c] *Department of Materials and Engineering, Henry Samueli School of Engineering and Applied Science, University of California, Los Angeles, CA 90095, USA*
[d] *Department of Chemistry and Biochemistry, University of California, Santa Barbara, CA 93106, USA*
[e] *Mechanical Engineering Simulation and Design Group, The Sirindhorn International Thai-German Graduate School of Engineering (TGGS), King Mongkut's University of Technology North Bangkok (KMUTNB), 1518 Pracharat 1 Road, Wongsawang, Bangsue, Bangkok 10800, Thailand*
[f] *California NanoSystems Institute, University of California, Los Angeles, CA 90095, USA*
[g] *Institute of the Environment and Sustainability, University of California, Los Angeles, CA 90095, USA*

GRAPHICAL ABSTRACT

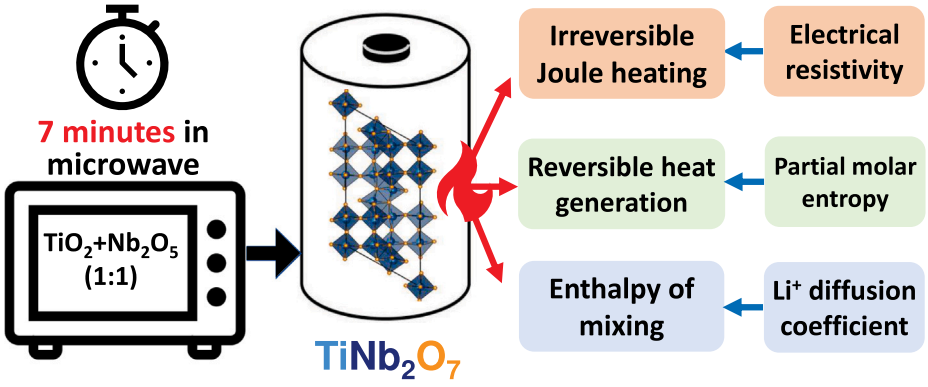

ARTICLE INFO

Keywords:
Lithium ion batteries
Reversible heat generation
Entropy
Microwave synthesis
Thermal signature
Lithium diffusion

ABSTRACT

The shear-phase compound $TiNb_2O_7$ has recently emerged as a safe and high-volumetric density replacement for graphite anodes in lithium ion batteries. An appealing feature of $TiNb_2O_7$ is that it retains capacity even at high cycling rates. Here, we demonstrate that phase pure and crystalline $TiNb_2O_7$ can be rapidly prepared using a high-temperature microwave synthesis method. Studies of the charging and discharging of this material, including through *operando* calorimetry, permit key thermodynamic parameters to be revealed. The nature of heat generation is dominated by Joule heating, which sensitively changes as the conductivity of the electrode increases with increasing lithiation. The enthalpy of mixing, obtained from *operando* calorimetry, is found to be small across the different degrees of lithiation, pointing to the high rate of lithium ion diffusion at the origin of rapid rate performance.

* Corresponding author at: Mechanical and Aerospace Engineering Department, Henry Samueli School of Engineering and Applied Science, University of California, Los Angeles, CA 90095, USA.
E-mail address: pilon@seas.ucla.edu (L. Pilon).

https://doi.org/10.1016/j.jpowsour.2021.229537
Received 13 October 2020; Received in revised form 15 December 2020; Accepted 17 January 2021

1. Introduction

Fast charging electrical energy storage devices with high energy density, compact size, and long-life have received significant research interest driven by the remarkable increase in demand for portable consumer electronics and electric vehicles (EV) [1–4]. In this context, lithium-ion batteries (LIBs) with high energy density and low environmental impact have received particular attention [5]. Graphite has been widely used as an anode material in LIBs owing to its low cost, structural stability upon cycling, and high energy density [6,7]. However, graphite anodes suffer from performance degradation over time caused by the formation of a passivating solid–electrolyte interface (SEI) layer due to its low operating voltage of 0.1 V (*versus* Li/Li^+) [8,9]. Furthermore, the plating of lithium on the SEI layer degrades the kinetics of the redox reaction thus limiting the charging rate of the LIBs [10,11]. Therefore, graphite anodes are not suitable for fast charging applications. To address the challenges associated with graphite anodes, many alternative transition metal oxides have been developed including TiO_2 [12–14], $LiCrTiO_4$ [15,16], and $Li_4Ti_5O_{12}$ [17–19]. In fact, $Li_4Ti_5O_{12}$ features an operating potential plateau of approximately 1.5 V (*versus* Li/Li^+) and has been a leading candidate due to its relatively abundant and non-toxic elements and its structural stability upon cycling [20]. However, $Li_4Ti_5O_{12}$ features relatively low specific capacity (~160 mAh/g) [11]. Recently, $TiNb_2O_7$ has been proposed as an alternative anode material [21]. Based on five lithium insertion per formula unit, $TiNb_2O_7$ has a theoretical specific capacity of 388 mAh/g and a theoretical volumetric capacity of 1680 mAh/cm^3, i.e., twice as large as that of graphite [22]. $TiNb_2O_7$ has been synthesized through different solid-state [21,23] and hydrothermal [24] methods. Unfortunately, these methods require long heat treatments. For instance, the conventional solid-state method requires heat treatment at temperature ≥ 1000 °C for approximately 24 h [21,23] while the hydrothermal method requires heat treatment at temperature ≥ 1100 °C for 12 h [24].

The present study aims to develop a fast, simple, and cost-effective synthesis method of $TiNb_2O_7$ for LIB anode electrodes. The synthesized materials and the associated electrodes were characterized by high-resolution synchrotron X-ray diffraction (XRD), conventional electrochemical methods, and potentiometric entropy measurement techniques. Finally, *operando* calorimetric measurements were used to deepen our understanding of the lithiation/delithiation process in $TiNb_2O_7$ electrodes and to investigate the associated heat generation upon cycling at high C-rates.

2. Background

Four main phenomena contribute to heat generation in LIBs including (i) Joule heating, (ii) reversible entropic heat generation, (iii) heat of mixing, and (iv) undesirable side reactions [25–28]. Joule heating corresponds to irreversible resistive losses in the battery with an associated heat generation rate expressed as $\dot{Q}_J(x,t) = R_I(x)I^2$ where $R_I(x)$ is the battery internal resistance at lithium composition x. Alternatively, $\dot{Q}_J(x,t)$ can be expressed as a function of the applied current I and the battery overpotential defined as the difference between the operating voltage $V(x,t)$ and the open circuit voltage $U_{ocv}(x,T)$, i.e. [25–28],

$$\dot{Q}_J(x,t) = I[V(x,t) - U_{ocv}(x,T)]. \tag{1}$$

The overpotential in the device can be interpreted as the voltage drop due to the LIB's internal resistance. The latter is influenced by many factors and their effects have been discussed extensively in the literature [29]. In brief, the battery internal resistance is known to increase with (i) increasing number of cycles [30,31], (ii) increasing charge-transfer resistance [32], (iii) decreasing ionic conductivity [32], and (iv) increasing electrolyte viscosity [33]. Additionally, the impact of changes in the state of charge (SOC) on the internal resistance upon lithiation/delithiation varies significantly with cell chemistry since the battery materials often experience phase transitions. The internal resistance of LIBs can be measured for different lithium compositions using *ex situ* techniques [34]. Even though these methods can be used to evaluate the changes in internal resistance at different SOC, it cannot capture the change in internal resistance during cycling. *Operando* calorimetry offers an alternative technique to evaluate the LIB's internal resistance during cycling.

The reversible entropic heat generation rate $\dot{Q}_{rev}(x,t)$ due to entropic changes in the electrode upon lithiation/delithiation can be expressed as [25–28]

$$\dot{Q}_{rev}(x,t) = IT\frac{\partial U_{ocv}(x,T)}{\partial T} = IT\frac{\bar{s}(x,T)}{nF}. \tag{2}$$

Here, $\bar{s}(x,T) = nF\partial U_{ocv}(x,T)/\partial T$ is the partial molar entropy of the cell, T is the temperature of the cell, n is the number of electrons transferred by a single ion, and F is the Faraday constant. Note that the derivative $\partial U_{ocv}(x,T)/\partial T$ is often termed as the entropic potential and varies significantly with the SOC and any phase transitions in the cell upon lithiation/delithiation [28].

The heat of mixing also known as enthalpy of mixing $\dot{Q}_{mix}(x,t)$ associated with ion concentration gradients caused by mass transfer resistance in the system can be written as [25–27]

$$\dot{Q}_{mix}(x,t) = -\int_{V_\infty}\sum_i [\bar{h}_i(x,T) - \bar{h}_i^{avg}(x,T)]\frac{\partial c_i}{\partial t}\mathrm{d}V. \tag{3}$$

Here, V_∞ is the volume of the cell, $\bar{h}_i(x,T)$ is the partial molar enthalpy of species i evaluated at the volume-averaged concentration at time t, and c_i is the local concentration of species i. For LIBs, the enthalpy of mixing can be further divided into four different contributions associated with ionic concentration gradients (i) across the electrolyte due to mass transfer, (ii) across the electrode due to non-uniform current distribution, (iii) within lithium vacancies in the electrode due to electrochemical reactions, and (iv) within the lithium ions intercalated into the electrode from electrochemical reactions [35,36]. Among these different contributions, the enthalpy of mixing caused by the concentration gradient of the intercalated lithium ions within the electrode is the most significant [27]. Note that $\dot{Q}_{mix}(x,t)$ is often negligible at low C-rates. However, $\dot{Q}_{mix}(x,t)$ has to be considered for fast charging battery applications since it can be significant at high C-rates [26]. In fact, a previous study [35] reported that the energy dissipated as enthalpy of mixing in a cell consisting of $LiAl_{0.2}Mn_{1.8}O_{4-\delta}F_{0.2}$ as the cathode, $LiPF_6$ in EC:DMC 1:1 v/v as the electrolyte, and lithium metal as the anode represented about 1.3% of the total energy dissipated as heat at C-rate of C/3. However, it reached to 52% at C-rate of 2C. Therefore, the enthalpy of mixing must be accounted for when considering heat generation in fast charging batteries.

Finally, the heat generation due to undesirable side reactions $\dot{Q}_{sr}(x,t)$ can be expressed as [25–27]

$$\dot{Q}_{sr}(x,t) = -\sum_i \Delta H_i \dot{r}_i(t) \tag{4}$$

where ΔH_i is the enthalpy of reaction of chemical reaction i occurring at reaction rate $\dot{r}_i(t)$. Previous studies on heat generation in LIBs have neglected $\dot{Q}_{sr}(x,t)$ [25–28]. In fact, the aging process of LIBs occurs at relatively slow rates [25] and the magnitude of $\dot{Q}_{sr}(x,t)$ is much smaller than that of $\dot{Q}_J(x,t)$, $\dot{Q}_{rev}(x,t)$, and $\dot{Q}_{mix}(x,t)$ under normal operation [26]. Overall, the total instantaneous heat generation rate $\dot{Q}_T(x,t)$ (in W) in the entire cell can be written as sum of all those four terms, i.e. [25–28],

$$\dot{Q}_T(x,t) = \dot{Q}_J(x,t) + \dot{Q}_{rev}(x,t) + \dot{Q}_{mix}(x,t) + \dot{Q}_{sr}(x,t). \tag{5}$$

Here, $\dot{Q}_T(x,t)$ is positive when heat is released by the cell and negative when heat is absorbed by the cell.

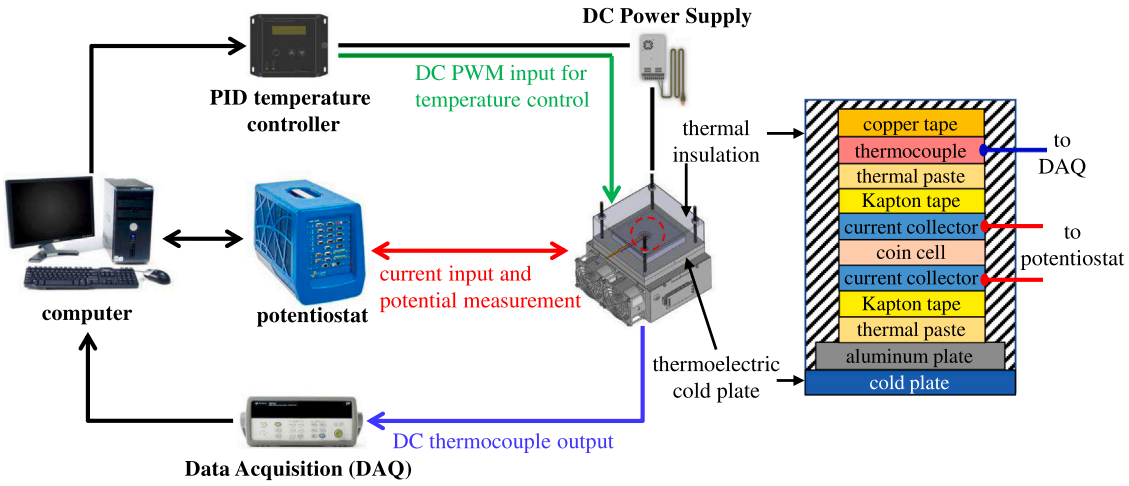

Fig. 1. Schematic of the experimental setup used for the potentiometric entropy measurement.

3. Materials and methods

3.1. Microwave synthesis of $TiNb_2O_7$

In this study, $TiNb_2O_7$ particles were synthesized using a fast and simple method consisting of a single heating step in a microwave oven under ambient atmosphere. First, the precursor powders TiO_2 (Aldrich Chemical Company, 99%) and Nb_2O_5 (Materion, 99.95%) were thoroughly ground together in stoichiometric quantities (1:1) using an agate mortar and pestle. The ground powder was then pressed into 250 mg to 300 mg pellets using a hand-operated arbor press. The pellets were placed on a small sacrificial powder layer of the same material inside of a 10 mL alumina crucible. This crucible was then nestled into a larger 20 mL alumina crucible filled with approximately 7 g of activated charcol covered in alumina fiberboard insulation, and placed off-center in a 1250 W microwave oven (Panasonic). This stack was heated at 90% of the total microwave power (i.e., 1125 W) for 7 to 8 min reaching temperatures around 1200 °C, as observed with a laser thermometer, immediately upon reaction completion. The insulation was removed, and the pellets were allowed to cool to room temperature. The produced crystalline $TiNb_2O_7$ particles required no additional processing prior to fabricating the electrode. Additional background on general microwave sample preparation can be found in Ref. [37].

3.2. Structural characterization

High resolution synchrotron X-ray diffraction measurements of the synthesized $TiNb_2O_7$ powder were collected at room temperature at the Advanced Photon Source at Argonne National Laboratories on beamline 11-BM-B using an average wavelength of 0.457856 Å. The $TiNb_2O_7$ powder sample was loaded into a Kapton capillary and both ends were sealed with clay. Rietveld refinement was performed with TOPAS [38], while VESTA [39] was used for crystal structure visualization.

3.3. Electrochemical testing

The electrodes were cast on copper foil using an 80:10:10 (wt%) ratio of active material ($TiNb_2O_7$), conductive carbon (TIMCAL SuperP), and polyvinylidene fluoride (Sigma Aldrich). The active material was ball-milled for 30 min in a 2 cm^3 canister with SuperP. This mixture was added to PVDF dissolved in 1-methyl-2-pyrrolidinone (Sigma Aldrich) to form a slurry and was mixed in a FlackTek speed mixer at 2000 rpm for 30 min. The slurry was cast onto a copper foil using a doctor blade set for 150 μm. Then, the film was dried overnight at 110 °C in a vacuum oven. The fabricated electrode was then punched into 10 mm diameter discs resulting in an active material loading of 5.6 mg/cm^2 and assembled into a coin cell configuration (MTI parts, 2032 SS casings) with 1 M of $LiPF_6$ in EC:DMC 1:1 v/v (Sigma Aldrich) as electrolyte and polished lithium metal (Sigma Aldrich) as the counter electrode with a 50 μm thick polypropylene/polyethylene separator (Celgard C380). Cyclic voltammetry (CV), galvanostatic cycling (GC), and galvanostatic intermittent titration technique (GITT) were performed on the coin cell in the voltage range of 1.0–3.0 V using a high accuracy potentiostat (Biologic, VSP-300). During GITT, each current pulse was applied for 1 min followed by a relaxation period of 30 min to measure the open circuit voltage $U_{ocv}(x,T)$ as a function of composition x in $Li_xTiNb_2O_7$ at constant temperature T = 20 °C. All potentials in this study are reported relative to Li/Li^+, and C-rates are defined with respect to the reduction of one electron per transition metal, e.g., 1C = 233 mAh/g.

3.4. Potentiometric entropy measurement

The partial molar entropy $\bar{s}(x,T)$ of the $TiNb_2O_7$ half-cell was measured as a function of lithium composition x using a potentiometric entropy measurement technique performed on a coin cell. The lithium metal counter electrode was considered as an infinite Li^+ reservoir with no lattice rearrangement upon lithiation/delithiation [40]. Therefore, the contribution of the lithium metal electrode to the partial molar entropy was assumed to be constant throughout the cycle [41,42]. The entropic potential of the $TiNb_2O_7$ coin cell $\partial U_{ocv}(x,T)/\partial T$ was measured to determine the partial molar entropy $\bar{s}(x,T)$ using Eq. (2).

Fig. 1 shows the schematic of the custom-made experimental setup assembled for potentiometric entropy measurements. The experimental setup consisted of a thermoelectric cold plate (TE technology, CP-121) whose temperature was measured by a type-K thermocouple (Omega, GG-KI-24S-200) via a data acquisition system (Keysight, Agilent 34972A). The temperature of the cold plate was controlled by a proportional–integral–derivative (PID) temperature controller (TE technology, TC-720). The coin cell and current collectors were wrapped with Kapton tape to prevent electrical contact with the thermoelectric cold plate. Thermal paste (Omega, OT-201-16) was applied between the thermoelectric cold plate and the wrapped coin cell to ensure good thermal contact. The type-K thermocouple was secured on top of the coin cell assembly with the thermal paste and covered by a copper tape for accurate temperature measurements. The entire setup was thermally insulated with Styrofoam to reduce heat losses to the surrounding and achieve precise control of the coin cell temperature.

The potentiometric entropy measurements consisted of imposing a series of constant current pulses at a C-rate of 2C for one minute at 20 °C each followed by a relaxation period of 90 min. During the relaxation, a step-like temperature profile was applied to the coin cell from

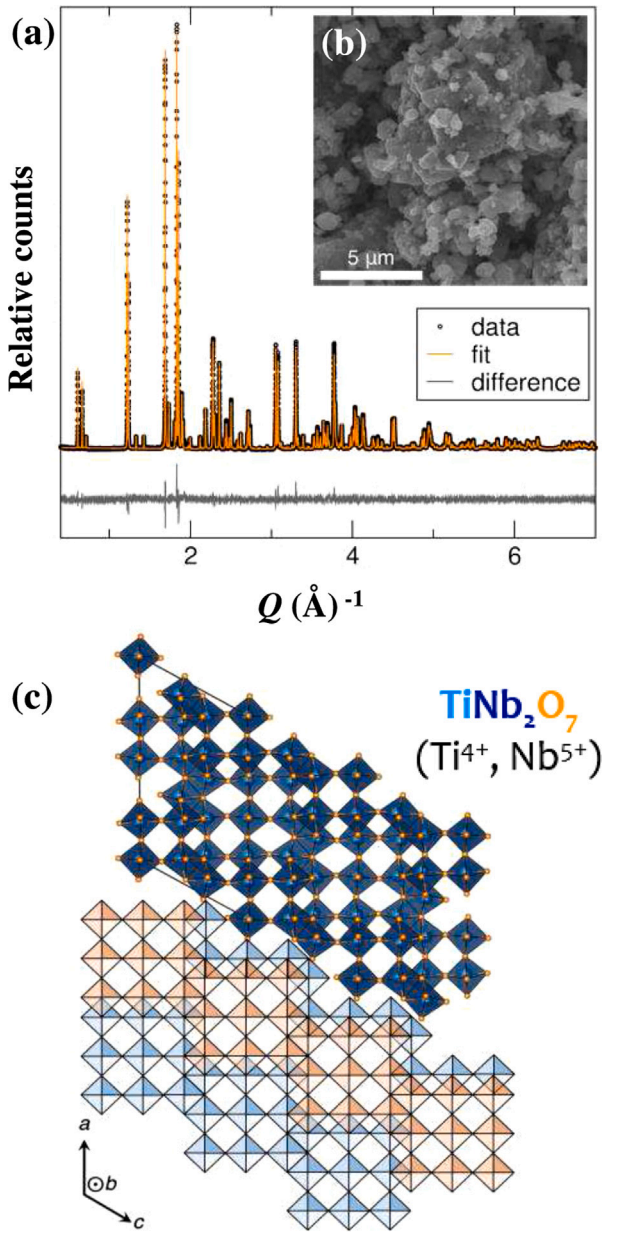

Fig. 2. (a) Synchrotron X-ray diffraction pattern and (b) SEM image of the $TiNb_2O_7$ particles synthesized by the proposed microwave method, (c) crystallographic structure of pure $TiNb_2O_7$. The two different colors used for the blocks of octahedra are used to indicate that they are offset in the b direction.

15 °C to 25 °C in 5 °C increments. The resulting voltage profile was recorded with the potentiostat (Biologic, VSP-300). Before recording the open circuit voltage $U_{ocv}(x,T)$ and imposing the next temperature step, we verified that the cell was in thermodynamic equilibrium by making sure that (i) the temperature difference between the cold plate and the top of the coin cell was less than 0.1 °C and (ii) the time rate of change of the open circuit voltage $\partial U_{ocv}/\partial t$ was less than 1 mV/h.

3.5. Operando isothermal calorimetry

The instantaneous heat generation rate in the $TiNb_2O_7$ half-cell was measured under galvanostatic cycling using a custom-made isothermal calorimeter previously described [43]. The $TiNb_2O_7$ electrode was cut into a 1 x 1 cm^2 square and assembled into a calorimetric cell with 1 M $LiPF_6$ in EC:DMC 1:1 v/v (Sigma Aldrich) as the electrolyte and polished lithium metal ribbon (Sigma Aldrich) as the counter electrode with a 50 μm thick Celgard C380 polypropylene/polyethylene separator. Based on the thermal analysis of a single electrode described in Supplementary Materials of Ref. [43], the heat generation rate $\dot{Q}_i(t)$ (in mW) at each electrode was equal to the heat transfer rate $q_i''(t)$ passing through the 1 × 1 cm^2 thermoelectric heat flux sensor (greenTEG, gSKIN-XP) such that [43],

$$\dot{Q}_i(t) = q_i''(t)A_i = \frac{\Delta V_i(t)}{S_i}A_i \qquad \text{with } i = + \text{ or } - \tag{6}$$

where A_i denotes the footprint area of the electrode (in cm^2) while S_i is the temperature-dependent sensitivity of the heat flux sensor provided by the manufacturer (in μV/(W/m^2)) while subscript "i" refers to either the cathode "+ " or anode "−". Here, ΔV_i is the voltage difference measured in each heat flux sensor in thermal contact with electrode "i". The total instantaneous heat generation rate in the entire device was the sum of the heat generation rate measured at each electrode, i.e., $\dot{Q}_T(t) = \dot{Q}_+(t) + \dot{Q}_-(t)$.

4. Results and discussion

4.1. Structural characterization

Fig. 2(a) shows a high resolution synchrotron X-ray diffraction (XRD) diagram of $TiNb_2O_7$ prepared using the previously described synthesis method. The XRD pattern was consistent with those prepared by conventional methods [23]. The pristine $TiNb_2O_7$ particles formed an electrically insulating white powder [44]. Fig. 2(b) shows a SEM image of the synthesized $TiNb_2O_7$ particles typically less than 5 μm (see also Supplementary Material) and smaller than the average particle size of 20 μm synthesized by solid state method [23]. Fig. 2(c) illustrates the crystallographic structure of pure $TiNb_2O_7$ featuring a Wadsley–Roth crystallographic shear structure similar to those of ReO_3 and PNb_9O_{25} [44]. Overall, in stark contrast to the more conventional synthesis methods of transition metal oxide $TiNb_2O_7$ [21,23,24], the proposed method offers a much faster alternative. In fact, in less than 10 min in a standard microwave oven, the same compound was synthesized without necessitating any additional purification or annealing steps. An additional benefit of the present microwave preparation method was that the shorter heating time resulted in smaller $TiNb_2O_7$ particles.

4.2. Electrochemical properties

Fig. 3(a) shows the cyclic voltammogram of a $TiNb_2O_7$ based electrode at different scan rates between 1.0 V and 3.0 V (vs. Li/Li^+). A sharp cathodic peak at 1.58 V and an anodic peak at 1.7 V were observed at scan rate of 0.1 mV/s. These two major peaks corresponded to the conversion of Nb^{5+}/Nb^{4+} and were consistent with previous reports [11,23,45,46]. In addition, one pair of shoulder peaks at 1.5 V for the cathodic sweep and at 1.62 V for the anodic sweep might be caused by different niobium states which are edge-shared octahedral and corner shared octahedral [23,45,46]. The pair of broad peaks in the potential range of 1.0 to 1.4 V may be caused by the Nb^{4+}/Nb^{3+} redox couple [23,45,46]. Another pair of a broad peaks in the potential range of 1.75 to 2.0 V was associated with the conversion of Ti^{4+}/Ti^{3+} [45,46]. In addition, Fig. 3(b) and (c) show the peak current I_{peak} values measured at different scan rates v for the cathodic peak, and anodic peak respectively. The b-value of the cathodic and anodic peaks were obtained by calculating the index of the power law fit of the I_{peak} versus scan rate v, i.e., $I_{peak} = av^b$. The b-value of the cathodic peak was found to be 0.78 and that of the anodic peak was 0.7. The b-values in the range of 0.7–0.8 suggest that the $TiNb_2O_7$ goes through a fast redox reaction with relatively low diffusion limitations.

Fig. 3(d) shows the capacity retention of $TiNb_2O_7$ at various C-rates for a potential window between 1.0 V and 3.0 V (vs. Li/Li^+). The

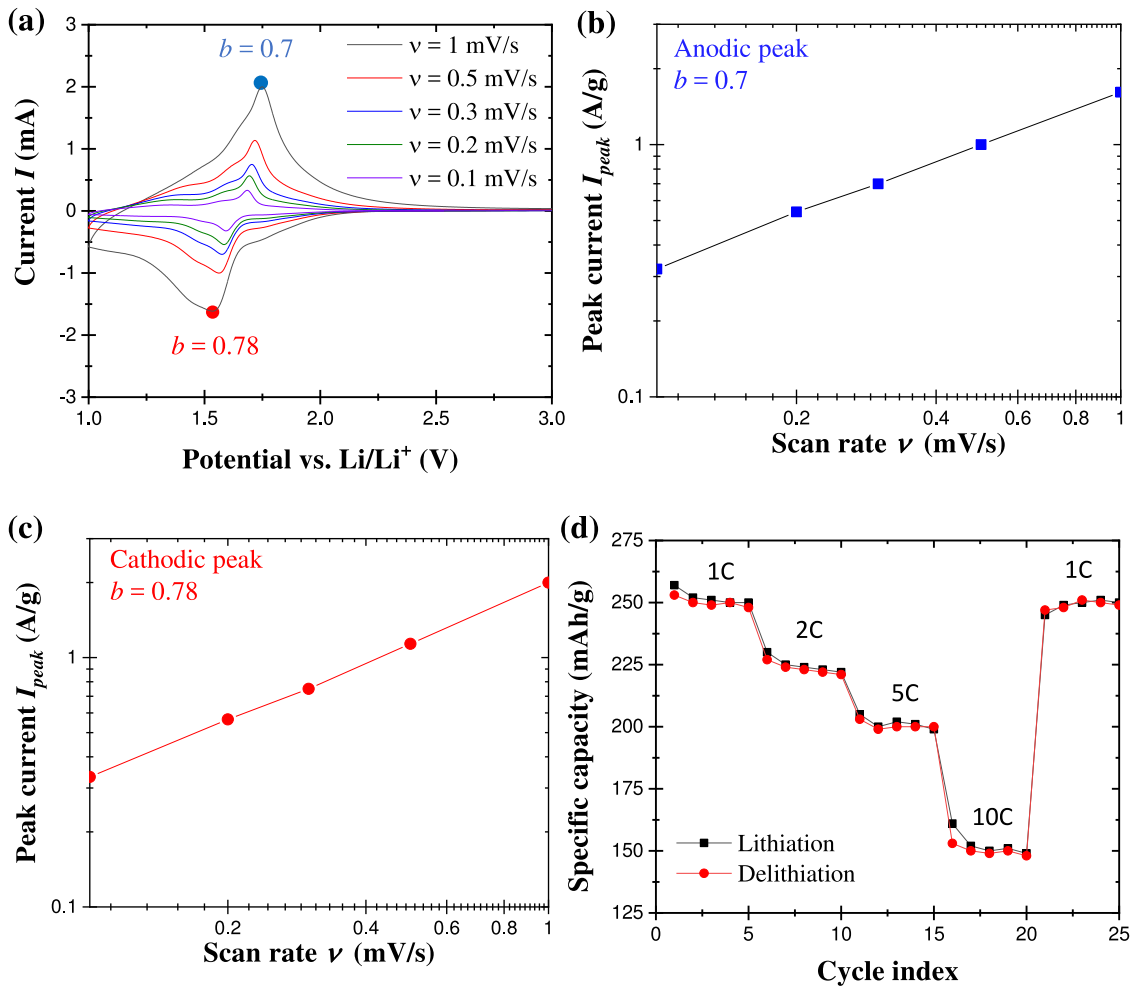

Fig. 3. (a) Cyclic voltammogram of $TiNb_2O_7$ half-cell cycled with a potential window ranging from 1.0 to 3.0 V vs. Li/Li^+ at different scan rates ν, (b) measured peak current I_{peak} as a function of ν for the anodic peak, and (c) for the cathodic peak, (d) specific capacity retention of the $TiNb_2O_7$ at various C-rates in the voltage range of 1.0–3.0 V.

theoretical capacity of $TiNb_2O_7$ is estimated to be 388 mAh/g upon 5 lithium ion insertion [21]. Here, the measured reversible capacity of the $TiNb_2O_7$ electrode was around 255 mAh/g at C-rate of 1C. At C-rate of 2C, the $TiNb_2O_7$ electrode provided up to 60% of its theoretical capacity while graphite anode can only provide 22% of its theoretical capacity for the same C-rate [47]. Furthermore, even at rate of 10 C, the $TiNb_2O_7$ electrode maintained 40% of its theoretical capacity and showed impressive reversibility over a number of cycles.

4.3. Partial molar entropy of $TiNb_2O_7$

Fig. 4(a) plots the cell voltage $V(x,t)$ and open circuit voltage $U_{ocv}(x,T)$ as functions of x composition in $Li_xTiNb_2O_7$ measured by GITT at C-rate of 2C and temperature T = 20 °C. It features three distinct regions apparent in the slope of the open circuit voltage curve during the incorporation process of Li^+ in $Li_xTiNb_2O_7$. The first sharp drop in $U_{ocv}(x,T)$ in the range $0.0 \leq x \leq 0.75$ was indicative of a homogeneous solid solution [11]. Then, the voltage plateau in the range $0.75 \leq x \leq 1.5$ corresponded to a two phase coexistence region, as discussed in the literature [11,21]. Finally, the shallow slope for $1.5 \leq x \leq 3.0$ corresponded to another homogeneous solid solution [11,21].

Fig. 4(b) shows the measured partial molar entropy $\bar{s}(x,T)$ and open circuit voltage $U_{ocv}(x,T)$ of the $TiNb_2O_7$ half-cell as functions of lithium composition x in $Li_xTiNb_2O_7$ during lithiation at 20 °C. The measurements were found to be in a good agreement with previous studies [22]. Indeed, $\bar{s}(x,T)$ was negative throughout the entire lithium composition upon lithium insertion. Therefore, the reversible entropic heat generation was expected to be strictly exothermic ($\dot{Q}_{rev} \geq 0$) during lithiation and endothermic ($\dot{Q}_{rev} \leq 0$) during delithiation. For $x < 0.75$, the entropy $\bar{s}(x,T)$ decreased rapidly upon insertion of lithium in the homogeneous solid solution forming a more ordered structure [22]. However, the entropy $\bar{s}(x,T)$ started to increase around x = 0.75 due to the transition from a homogeneous solid solution to a two-phase coexistence region. The *in situ* XRD data reported in literature [11,48] shows that all the $TiNb_2O_7$ reflections were maintained upon lithiation/delithiation for all values of x. Therefore, the structure of both homogeneous solid solution phases was in the monoclinic phase with the identical C/2m space group and $TiNb_2O_7$ did not experience crystallographic phase transition [48]. However, $\bar{s}(x,T)$ experienced fluctuation in the composition range $0.75 \leq x \leq 1.5$ corresponding to a two-phase coexistence region. Since a crystallographic phase change did not occur, the observed fluctuation in $\bar{s}(x,T)$ was influenced by the intralayer lithium ordering rather than by a first order phase transition. This type of tilde shape entropy change was first observed by Dahn and Haering [49] upon lithiation of TiS_2. It occurs when it is energetically favorable for the inserted lithium ions in the lattice to arrange themselves in the vacancies in a more ordered fashion than being randomly inserted for further insertion of lithium ions [50]. This intralayer lithium reordering corresponds to rapid lithium mobility within the Wadsley–Roth block motifs down the tunnels along the *b*-axis and also between the lithium vacancy sites with higher activation energy and that with lower activation energy along the intrablock tunnels as reported in a previous density functional theory (DFT) study [44]. For $x > 1.5$, $\bar{s}(x,T)$ was nearly constant within a range of

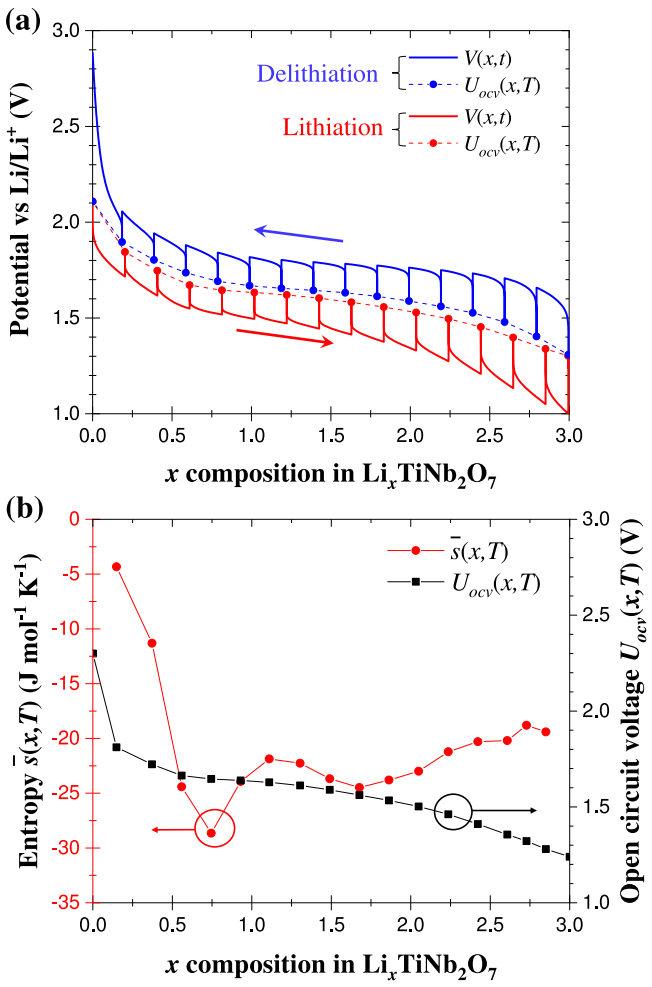

Fig. 4. Galvanostatic intermittent titration technique (GITT) curve plotting (a) cell potential $V(x,t)$ and open circuit voltage $U_{ocv}(x,T)$ during delithiation and lithiation as functions of lithium composition x in $Li_xTiNb_2O_7$; (b) partial molar entropy $\bar{s}(x,T)$ and open circuit voltage $U_{ocv}(x,T)$ as functions of x during lithiation. Both measurements were taken at C-rate of 2C and temperature T = 20 °C.

−20 to −25 J/mol K indicating the filling of leftover vacancy sites in the shear structure of the homogeneous solid solution [22].

4.4. Heat generation of $TiNb_2O_7$

Fig. 5(a) plots the irreversible Joule heat generation rate $\dot{Q}_J(x,t)$ during lithiation and delithiation calculated from Eq. (1) based on the imposed current I, the cell voltage $V(x,t)$ measured in the calorimeter under galvanostatic cycling at C-rate of 2C, and the open circuit voltage $U_{ocv}(x,T)$ measured by GITT at 20 °C. The change observed in $\dot{Q}_J(x,t)$ could be attributed to changes in the electrical resistivity of $TiNb_2O_7$ upon lithiation. Indeed, $TiNb_2O_7$ is an insulator in its unlithiated state, and exhibits very large electrical resistivity ~ 10^9 Ω cm [51]. However, upon lithiation to $Li_{0.25}TiNb_2O_7$, the electrical resistivity decreases by seven orders of magnitude to ~ 50 Ω cm [51]. This change in electrical resistivity was well captured by the sharp drop in $\dot{Q}_J(x,t)$ in the composition range $0 \le x \le 0.9$. Furthermore, the electrical resistivity slightly increased again upon further lithium ion insertion. In fact, the electrical resistivity was measured to be ~ 700 Ω cm for $LiTiNb_2O_7$ and ~ 2000 Ω cm for $Li_{2.5}TiNb_2O_7$ [51]. This increase in the electrical resistivity of $Li_xTiNb_2O_7$ was also captured by $\dot{Q}_J(x,t)$ for composition x in the range $0.9 \le x \le 3$. However, $\dot{Q}_J(x,t)$ during delithiation differed from that during lithiation possibly due to the difference in mass transfer resistance associated with Li^+ diffusion in the electrode.

Moreover, Fig. 5(b) shows the reversible heat generation rate $\dot{Q}_{rev}(x,t)$ during lithiation, and delithiation estimated using Eq. (2) based on the measured entropic potential $\partial U_{ocv}(x,T)/\partial T$. Here, $\dot{Q}_{rev}(x,t)$ was exothermic (i.e., positive) upon lithiation and endothermic (i.e., negative) upon delithiation. The effect of $\dot{Q}_{rev}(x,t)$ became significant as $Li_xTiNb_2O_7$ transitioned from a homogeneous solid solution to two coexisting solid phases around $x \simeq 0.75$. After the sharp change, $\dot{Q}_{rev}(x,t)$ remained fairly constant for the rest of the lithiation process. Note also that integrating $\dot{Q}_{rev}(x,t)$ over an entire cycle yielded nearly zero, confirming the reversible nature of this heat generation mechanism.

Fig. 6(a) and (b) plot the instantaneous heat generation rate $\dot{Q}_T(x,t)$ measured in the calorimeter cell at C-rate of 2C and T = 20 °C as a function of x in $Li_xTiNb_2O_7$. The sum of $\dot{Q}_J(x,t) + \dot{Q}_{rev}(x,t)$ was in relatively good agreement with the measured total heat generation rate $\dot{Q}_T(x,t)$. Assuming that the effect of heat generation due to side reactions $\dot{Q}_{sr}(x,t)$ was negligible [25–27], the difference between $\dot{Q}_T(x,t)$, and the sum $\dot{Q}_J(x,t) + \dot{Q}_{rev}(x,t)$ corresponded to the enthalpy of mixing, i.e., $\dot{Q}_{mix}(x,t) = \dot{Q}_T(x,t) - \dot{Q}_J(x,t) - \dot{Q}_{rev}(x,t)$ [Eq. (4)]. The heat dissipated due to enthalpy of mixing upon relaxation of quasi-steady state concentration gradients formed upon cycling was reported to be inversely proportional to the square of the apparent diffusion coefficient [35]. In fact, the apparent diffusion coefficient of lithium into the electrode, $D_{Li^+}(x)$ can be estimated by combining GITT and Fick's second law according to [52]

$$D_{Li^+}(x,T) = \frac{4}{\pi\tau}\left(\frac{V}{A}\right)^2\left(\frac{\Delta U_{ocv}(x,T)}{\Delta V_t(x)}\right)^2. \quad (7)$$

Here, τ is the duration of the GITT current pulse, A and V are the surface area and the volume of the electrode, $\Delta V_t(x)$ is the change in the cell potential as a result of the imposed current pulses excluding the IR drop at the beginning of the current pulse, and $\Delta U_{ocv}(x,T)$ is the change in the open circuit voltage between two consecutive current pulses. Fig. 6(c) shows the apparent diffusion coefficient of Li^+ in the electrode $D_{Li^+}(x)$ measured as a function of x in $Li_xTiNb_2O_7$ at 20 °C. It reached a minimum of 8 × 10^{-12} cm^2/s at $x_{min} \simeq 0.8$ during lithiation and at $x_{min} \simeq 1.4$ during delithiation. Interestingly, these values of x_{min} corresponded closely to the bounds of the voltage plateau (at U_{ocv} = 1.6 V) observed in the GITT curve (Fig. 4). This indicates that the very sharp decrease in $D_{Li^+}(x)$ was caused by the transition from a homogeneous solid solution phase reaction to a two-phase coexistence region [53]. In addition, this change in the apparent diffusion coefficient was also observed with the enthalpy of mixing $\dot{Q}_{mix}$. During the lithiation process, a significant drop in $D_{Li^+}(x,T)$ was observed for $0.4 \le x \le 0.8$. This contributed to an increase in the enthalpy of mixing $\dot{Q}_{mix}(x,t)$ and to its local maximum highlighted in Fig. 6(d). Similarly, the sharp decrease in $D_{Li^+}(x,T)$ during delithiation between $2.25 \ge x \ge 1.4$ correlated with an increase in the enthalpy of mixing and the local maximum highlighted in Fig. 6(d).

A recent experimental study demonstrated that the net electrical energy losses due to the hysteretic voltage profile upon cycling were dissipated as Joule heating at a low C-rate [26]. By operating at a C-rate of C/10, the authors were able to neglect the effect of enthalpy of mixing [26]. However, the latter can be significant in fast charging batteries operating under high currents [35]. Here, the net electrical energy losses ΔE_e (in J) between the electrical energy provided during charging and that recovered during discharging was illustrated in the hysteric voltage $V(x,t)$ and expressed as [26]

$$\Delta E_e = \oint_{cycle} V(x,t)\mathrm{d}q \quad (8)$$

where q is the charge transferred upon electrochemical reaction. The total thermal energy dissipated Q_T (in J) as well as the heat dissipated in the form of Joule heating Q_J and enthalpy of mixing Q_{mix} were calculated according to [26]

$$Q_i = \oint_{cycle} \dot{Q}_i(x,t)\mathrm{d}t \quad \text{with } i = T,\ J,\ rev, \text{or } mix \quad (9)$$

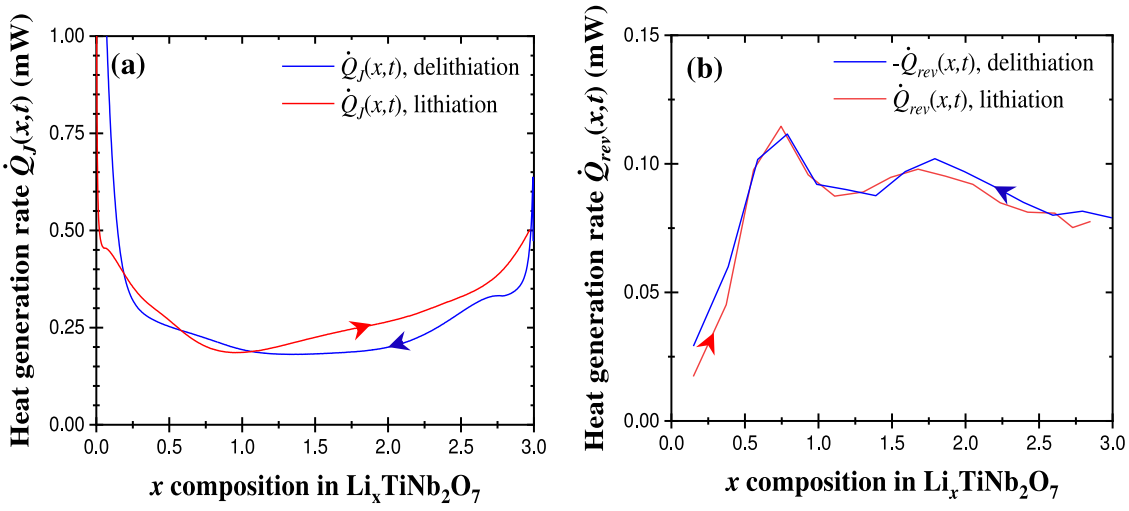

Fig. 5. (a) Irreversible Joule heat generation rate $\dot{Q}_J(x,t)$ during lithiation, and delithiation [Eqs. (1)], and (b) reversible heat generation rate $\dot{Q}_{rev}(x,t)$ during lithiation and delithiation [Eqs. (2)] as functions of lithium composition x in $Li_xTiNb_2O_7$ at temperature T = 20 °C.

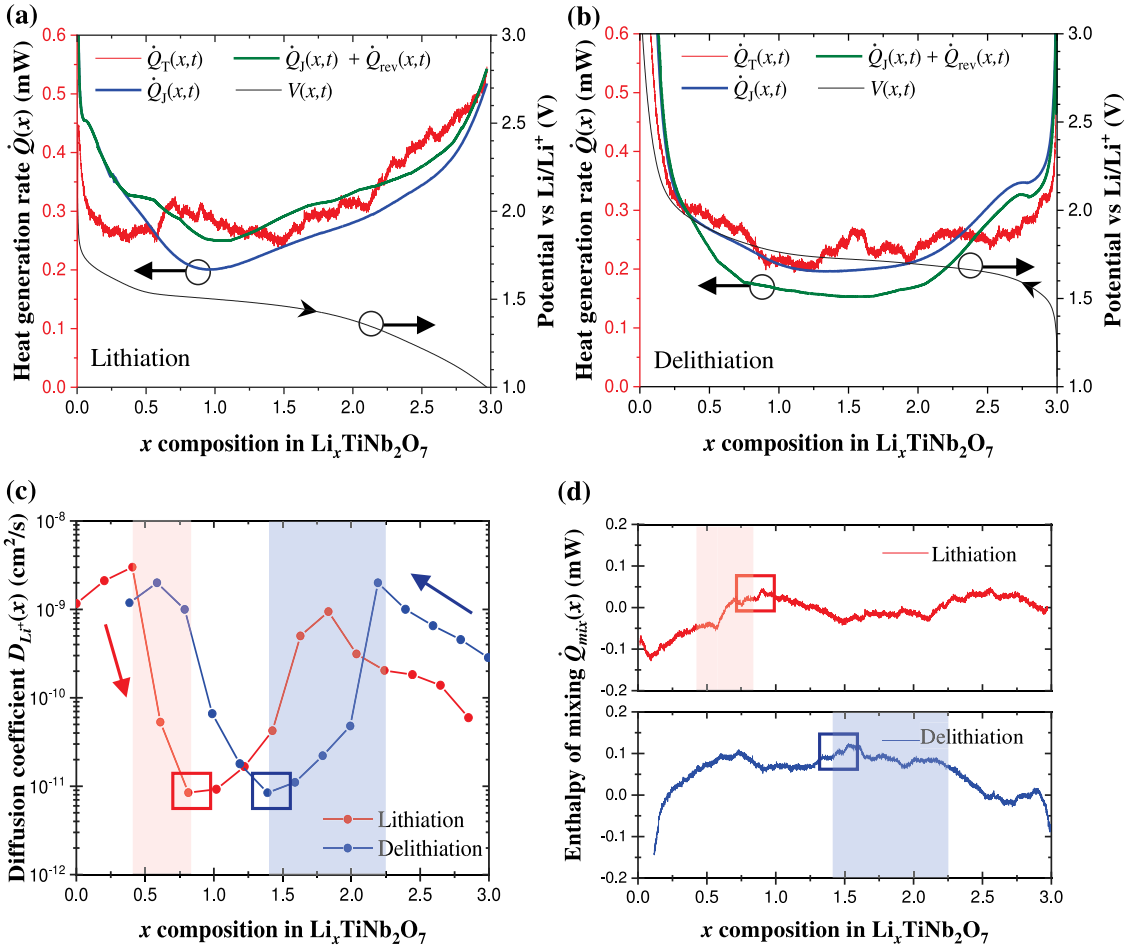

Fig. 6. Heat generation rates $\dot{Q}_T(x,t)$, $\dot{Q}_J(x,t)$, $\dot{Q}_J(x,t)+\dot{Q}_{rev}(x,t)$ [Eqs. (1), (2), (5)] and cell voltage $V(x,t)$ measured upon (a) lithiation, (b) delithiation at C-rate of 2C at 20 °C. (c) Apparent diffusion coefficient D_{Li^+} of lithium ion in $Li_xTiNb_2O_7$ and (d) enthalpy of mixing $\dot{Q}_{mix}(x,t) = \dot{Q}_T(x,t) - [\dot{Q}_J(x,t) + \dot{Q}_{rev}(x,t)]$ as functions of lithium composition x in $Li_xTiNb_2O_7$ at temperature T = 20 °C.

Fig. 7 presents the electrical energy losses ΔE_e over the first five cycles and the total thermal energy dissipated Q_T along with that due to Joule heating Q_J during lithiation and delithiation. The experimental error associated with Q_T was calculated based on the sensitivity of the heat flux sensor and on the precision of the data acquisition system (DAQ). Fig. 7 indicates that ΔE_e increased upon cycling possibly due to the associated increase in the internal resistance [30,31]. More importantly, ΔE_e fell within 2% of the measured total thermal energy Q_T generated per cycle, i.e., the electrical energy losses were dissipated entirely in the form of heat, i.e., $\Delta E_e = Q_T$. In addition, the irreversible

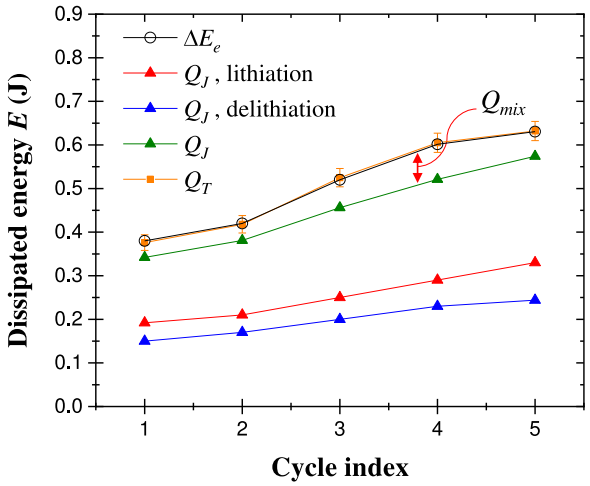

Fig. 7. Net electrical energy losses ΔE_e and total thermal energy dissipated Q_T for the first five charging–discharging cycles as well as that due to Joule heating Q_J during lithiation and delithiation. The enthalpy of mixing corresponds to $Q_{mix} = Q_T - Q_J = \Delta E_e - Q_J$.

Joule heating during lithiation was larger than that during delithiation due to the slower kinetics of lithiation characterized by a smaller apparent diffusion coefficient compared to delithiation resulting in a larger overpotential [54]. Since $Q_{rev} \simeq 0$, the difference between Q_T and Q_J represented the heat dissipated as enthalpy of mixing Q_{mix}. Over the first five cycles, thermal losses Q_T and Q_J increased as cycling proceeded. This can be attributed to the increase in the internal resistance with cycling possibly due to the mechanical degradation and growth of the SEI layer on the $TiNb_2O_7$ electrode [30,31]. Nevertheless, the enthalpy of mixing remained nearly constant regardless of the cycle number and contributed only 15% of the total energy dissipated. By contrast, calculations based on isothermal calorimetry on $LiAl_{0.2}Mn_{1.8}O_{4-\delta}F_{0.2}$ showed that the energy dissipated in the form of enthalpy of mixing was 52% of total dissipated heat at the same rate with the same electrolyte and counter electrode [35]. The present results indicate that the heat dissipation due to the enthalpy of mixing remained small in the calorimeter cell even at a C-rate of 2C which is very promising for fast charging battery applications.

5. Conclusion

This paper reports a fast, simple, and inexpensive synthesis method of small $TiNb_2O_7$ particles, requiring a mere 7 to 8 min in a microwave oven under an ambient atmosphere. This preparation method presents new opportunities for reducing the production costs and synthesis times of promising LIB anode with excellent performance at high C-rates. The synthesized $TiNb_2O_7$ particles were smaller than those synthesized with conventional solid state methods. Entropy measurements combined with previous *in situ* XRD measurements [11,48] established the occurrence of intralayer lithium ordering enabling the fast charging of $TiNb_2O_7$. In addition, the heat generation rate due to Joule heating varied widely during lithiation and delithiation and dominated the energy losses during cycling at C-rate of 2C. Such calorimetric measurements can further provide insight into changes in the electrical conductivity of batteries for different SOC upon cycling. Furthermore, the enthalpy of mixing remained small even at high C-rates and correlated with changes in the measured apparent diffusion coefficient of Li^+ in the $Li_xTiNb_2O_7$ electrode upon lithiation/delithiation. These results establish that $TiNb_2O_7$ constitutes an excellent anode material for fast charging battery applications.

CRediT authorship contribution statement

Sun Woong Baek: Conceptualization, Investigation, Formal analysis, Data curation, Visualization, Writing - original draft, Writing - review & editing. **Kira E. Wyckoff:** Conceptualization, Investigation, Visualization, Writing - original draft, Writing - review & editing. **Danielle M. Butts:** Investigation, Formal analysis. **Jadon Bienz:** Investigation. **Ampol Likitchatchawankun:** Conceptualization, Writing - review & editing. **Molleigh B. Preefer:** Investigation. **Matevž Fra-jnkovič:** Investigation. **Bruce S. Dunn:** Supervision, Conceptualization. **Ram Seshadri:** Supervision, Conceptualization. **Laurent Pilon:** Supervision, Conceptualization, Project administration, Writing - review & editing.

Declaration of competing interest

The authors declare that they have no known competing financial interests or personal relationships that could have appeared to influence the work reported in this paper.

Acknowledgments

This work was supported as part of the Center for Synthetic Control Across Length-scales for Advancing Rechargeables (SCALAR), an Energy Frontier Research Center funded by the U.S. Department of Energy, Office of Science, Basic Energy Sciences under Award # DE-SC0019381. The MRL Shared Experimental Facilities are supported by the MRSEC Program of the NSF under Award No. DMR 1720256; a member of the NSF-funded Materials Research Facilities Network (www.mrfn.org).

Appendix A. Supplementary data

Supplementary material related to this article can be found online at https://doi.org/10.1016/j.jpowsour.2021.229537.

References

[1] J.A. Rogers, Electronics for the human body, JAMA 313 (6) (2015) 561–562.
[2] H. Nishide, K. Oyaizu, Toward flexible batteries, Science 319 (5864) (2008) 737–738.
[3] H. Guo, M.-H. Yeh, Y. Zi, Z. Wen, J. Chen, G. Liu, C. Hu, Z.L. Wang, Ultralight cut-paper-based self-charging power unit for self-powered portable electronic and medical systems, ACS Nano 11 (5) (2017) 4475–4482.
[4] A. Meintz, J. Zhang, R. Vijayagopal, C. Kreutzer, S. Ahmed, I. Bloom, A. Burnham, R.-B. Carlson, F. Dias, E.-J. Dufek, J. Francfort, K. Hardy, A.-N. Jansen, M. Keyser, A. Markel, C. Michelbacher, M. Mohanpurkar, A. Pesaran, D. Scoffield, M. Shirk, T. Stephens, T. Tanim, Enabling fast charging – vehicle considerations, J. Power Sources 367 (5) (2017) 216–227.
[5] M. Walter, M.V. Kovalenko, K.V. Kravchyk, Challenges and benefits of post-lithium-ion batteries, New J. Chem. 44 (5) (2020) 1677–1683.
[6] S. Flandrois, B. Simon, Carbon materials for lithium-ion rechargeable batteries, Carbon 37 (2) (1999) 165–180.
[7] E. Peled, C. Menachem, D. Bar-Tow, A. Melman, Improved graphite anode for lithium-ion batteries chemically bonded solid electrolyte interface and nanochannel formation, J. Electrochem. Soc. 143 (1) (1996) L4–L7.
[8] J.B. Goodenough, Y. Kim, Challenges for rechargeable li batteries, Chem. Mater. 22 (3) (2010) 587–603.
[9] D. Aurbach, B. Markovsky, I. Weissman, E. Levi, Y. Ein-Eli, On the correlation between surface chemistry and performance of graphite negative electrodes for Li ion batteries, Electrochim. Acta 45 (1–2) (1999) 57–86.
[10] K. Amine, I. Belharouak, Z. Chen, T. Tran, H. Yumoto, N. Ota, S.-T. Myung, Y.-K. Sun, Nanostructured anode material for high-power battery system in electric vehicles, Adv. Mater. 22 (28) (2010) 3052–3057.
[11] B. Guo, X. Yu, X.-G. Sun, M. Chi, Z.-A. Qiao, J. Liu, Y.-S. Hu, X.-Q. Yang, J.B. Goodenough, S. Dai, A long-life lithium-ion battery with a highly porous $TiNb_2O_7$ anode for large-scale electrical energy storage, Energy Environ. Sci. 7 (7) (2014) 2220–2226.
[12] H. Liu, W. Li, D. Shen, D. Zhao, G. Wang, Graphitic carbon conformal coating of mesoporous TiO_2 hollow spheres for high-performance lithium ion battery anodes, J. Am. Chem. Soc. 137 (40) (2015) 13161–13166, 6.

[13] B.-L. He, B. Dong, H.-L. Li, Preparation and electrochemical properties of Ag-modified TiO_2 nanotube anode material for lithium–ion battery, Electrochem. Commun. 9 (3) (2007) 425–430.

[14] J. Wang, Y. Zhou, Y. Hu, R. O'Hayre, Z. Shao, Facile synthesis of nanocrystalline TiO_2 mesoporous microspheres for lithium-ion batteries, J. Phys. Chem. C 115 (5) (2011) 2529–2536.

[15] V. Aravindan, W. Chuiling, S. Madhavi, High power lithium-ion hybrid electrochemical capacitors using spinel $LiCrTiO_4$ as insertion electrode, J. Mater. Chem. 22 (31) (2012) 16026–16031.

[16] X. Feng, C. Shen, N. Ding, C. Chen, Lithium chromium oxide modified spinel $LiCrTiO_4$ with improved electrochemical properties, J. Mater. Chem. 22 (39) (2012) 20861–20865.

[17] K.-S. Park, A. Benayad, D.-K. Kang, S.-G. Doo, Nitridation-driven conductive $Li_4Ti_5O_{12}$ for lithium ion batteries, J. Am. Chem. Soc. 130 (45) (2008) 14930–14931.

[18] L. Zhao, Y.-S. Hu, H. Li, Z. Wang, L. Chen, Porous $Li_4Ti_5O_{12}$ coated with N-doped carbon from ionic liquids for Li-ion batteries, Adv. Mater. 23 (11) (2011) 1385–1388.

[19] J. Huang, Z. Jiang, The preparation and characterization of $Li_4Ti_5O_{12}$/carbon nano-tubes for lithium ion battery, Electrochim. Acta 53 (26) (2008) 7756–7759.

[20] B. Zhao, R. Ran, M. Liu, Z. Shao, A comprehensive review of $Li_4Ti_5O_{12}$-based electrodes for lithium-ion batteries: The latest advancements and future perspectives, Mater. Sci. Eng. R 98 (2015) 1–71.

[21] J.-T. Han, Y.-H. Huang, J.B. Goodenough, New anode framework for rechargeable lithium batteries, Chem. Mater. 23 (8) (2011) 2027–2029.

[22] N. Takami, K. Ise, Y. Harada, T. Iwasaki, T. Kishi, K. Hoshina, High-energy, fast-charging, long-life lithium-ion batteries using $tinb_2o_7$ anodes for automotive applications, J. Power Sources 396 (2018) 429–436.

[23] X. Lu, Z. Jian, Z. Fang, L. Gu, Y.-S. Hu, W. Chen, Z. Wang, L. chen, Atomic-scale investigation on lithium storage mechanism in $TiNb_2O_7$, Energy Environ. Sci. 4 (8) (2011) 2638–2644.

[24] K. Ise, S. Morimoto, Y. Harada, N. Takami, Large lithium storage in highly crystalline $TiNb_2O_7$ nanoparticles synthesized by a hydrothermal method as anodes for lithium-ion batteries, Solid State Ion. 320 (2018) 7–15.

[25] G. Liu, M. Ouyang, L. Lu, J. Li, X. Han, Analysis of the heat generation of lithium-ion battery during charging and discharging considering different influencing factors, J. Thermal Anal. Calorim. 116 (2) (2014) 1001–1010.

[26] G. Assat, S.L. Glazier, C. Delacourt, J.-M. Tarascon, Probing the thermal effects of voltage hysteresis in anionic redox-based lithium-rich cathodes using isothermal calorimetry, Nat. Energy 4 (8) (2019) 647–656.

[27] J. Newman, K.E. Thomas, H. Hafezi, D.R. Wheeler, Modeling of lithium-ion batteries, J. Power Sources 119 (2003) 838–843.

[28] D. Bernardi, E. Pawlikowski, J. Newman, A general energy balance for battery systems, J. Electrochem. Soc. 132 (1) (1985) 5–12.

[29] B. Yang, H. Zhang, L. Yu, W. Fan, D. Huang, Lithium difluorophosphate as an additive to improve the low temperature performance of $LiNi_{0.5}Co_{0.2}Mn_{0.3}O_2$/graphite cells, Electrochim. Acta 221 (2016) 107–114.

[30] M. Ecker, J.B. Gerschler, J. Vogel, S. Käbitz, F. Hust, P. Dechent, D.U. Sauer, Development of a lifetime prediction model for lithium-ion batteries based on extended accelerated aging test data, J. Power Sources 215 (2012) 248–257.

[31] D. Andre, M. Meiler, K. Steiner, C. Wimmer, T. Soczka-Guth, D. Sauer, Characterization of high-power lithium-ion batteries by electrochemical impedance spectroscopy. I. Experimental investigation, J. Power Sources 196 (12) (2011) 5334–5341.

[32] S. Ma, M. Jiang, P. Tao, C. Song, J. Wu, J. Wang, T. Deng, W. Shang, Temperature effect and thermal impact in lithium-ion batteries: A review, Prog. Natural Sci. Mater. Int. 28 (6) (2018) 653–666.

[33] T. Tsujikawa, K. Yabuta, T. Matsushita, T. Matsushima, K. Hayashi, M. Arakawa, Characteristics of lithium-ion battery with non-flammable electrolyte, J. Power Sources 189 (1) (2009) 429–434.

[34] S. Zhao, F. Wu, L. Yang, L. Gao, A.F. Burke, A measurement method for determination of dc internal resistance of batteries and supercapacitors, Electrochem. Commun. 12 (2) (2010) 242–245.

[35] K.E. Thomas, J. Newman, Thermal modeling of porous insertion electrodes, J. Electrochem. Soc. 150 (2) (2003) A176–A192.

[36] K.E. Thomas, J. Newman, Heats of mixing and of entropy in porous insertion electrodes, J. Power Sources 119 (2003) 844–849.

[37] E.E. Levin, J.H. Grebenkemper, T.M. Pollock, R. Seshadri, Protocols for high temperature assisted-microwave preparation of inorganic compounds, Chem. Mater. 31 (18) (2019) 7151–7159.

[38] A.A. Coelho, TOPAS and TOPAS-academic: an optimization program integrating computer algebra and crystallographic objects written in C^{++}, J. Appl. Crystallogr. 51 (1) (2018) 210–218.

[39] K. Momma, F. Izumi, VESTA 3 for three-dimensional visualization of crystal, volumetric and morphology data, J. Appl. Crystall. 44 (6) (2011) 1272–1276.

[40] V.V. Viswanathan, D. Choi, D. Wang, W. Xu, S. Towne, R.E. Williford, J.-G. Zhang, J. Liu, Z. Yang, Effect of entropy change of lithium intercalation in cathodes and anodes on li-ion battery thermal management, J. Power Sources 195 (11) (2010) 3720–3729.

[41] X.-F. Zhang, Y. Zhao, Y. Patel, T. Zhang, W.-M. Liu, M. Chen, G.J. Offer, Y. Yan, Potentiometric measurement of entropy change for lithium batteries, Phys. Chem. Chem. Phys. 19 (15) (2017) 9833–9842.

[42] S. Schlueter, R. Genieser, D. Richards, H.E. Hoster, M.P. Mercer, Quantifying structure dependent responses in Li-ion cells with excess Li spinel cathodes: matching voltage and entropy profiles through mean field models, Phys. Chem. Chem. Phys. 20 (33) (2018) 21417–21429.

[43] O. Munteshari, J. Lau, A. Krishnan, B.S. Dunn, L. Pilon, Isothermal calorimeter for measurements of time-dependent heat generation rate in individual supercapacitor electrodes, J. Power Sources 374 (2018) 257–268.

[44] K.J. Griffith, I.D. Seymour, M.A. Hope, M.M. Butala, L.K. Lamontagne, M.B. Preefer, C.P. Kocer, G. Henkelman, A.J. Morris, M.J. Cliffe, Ionic and electronic conduction in $TiNb_2O_7$, J. Am. Ceram. Soc. 141 (42) (2019) 16706–16725.

[45] H. Li, L. Shen, G. Pang, S. Fang, H. Luo, K. Yang, X. Zhang, $TiNb_2O_7$ nanoparticles assembled into hierarchical microspheres as high-rate capability and long-cycle-life anode materials for lithium ion batteries, Nanoscale 7 (2) (2015) 619–624.

[46] X. Wang, G. Shen, Intercalation pseudo-capacitive $TiNb_2O_7$@ carbon electrode for high-performance lithium ion hybrid electrochemical supercapacitors with ultrahigh energy density, Nano Energy 15 (2015) 104–115.

[47] H.-T. Kwon, J.-H. Kim, K.-J. Jeon, C.-M. Park, Co_xP compounds: electrochemical conversion/partial recombination reaction and partially disproportionated nanocomposite for Li-ion battery anodes, RSC Adv. 4 (81) (2014) 43227–43234.

[48] H. Yu, H. Lan, L. Yan, S. Qian, X. Cheng, H. Zhu, N. Long, M. Shui, J. Shu, $TiNb_2O_7$ hollow nanofiber anode with superior electrochemical performance in rechargeable lithium ion batteries, Nano Energy 38 (2017) 109–117.

[49] J. Dahn, R.R. Haering, Lithium intercalation in TiS_2, Mater. Res. Bull. 14 (10) (1979) 1259–1262.

[50] N.S. Hudak, L.E. Davis, G. Nagasubramanian, Cycling-induced changes in the entropy profiles of lithium cobalt oxide electrodes, J. Electrochem. Soc. 162 (3) (2015) A315–A321.

[51] W. Xing, L.-E. Kalland, Z. Li, R. Haugsrud, Defects and transport properties in $TiNb_2O_7$, J. Am. Ceram. Soc. 96 (12) (2013) 3775–3781.

[52] W. Weppner, R.A. Huggins, Determination of the kinetic parameters of mixed-conducting electrodes and application to the system Li_3Sb, J. Electrochem. Soc. 124 (10) (1977) 1569–1578.

[53] R. Inada, R. Kumasaka, S. Inabe, T. Tojo, Y. Sakurai, Li^+ insertion/extraction properties for $TiNb_2O_7$ single particle characterized by a particle-current collector integrated microelectrode, J. Electrochem. Soc. 166 (3) (2019) A5157–A5162.

[54] B. Babu, M.M. Shaijumon, Studies on kinetics and diffusion characteristics of lithium ions in $TiNb_2O_7$, Electrochim. Acta 345 (10) (2020) 136208.